Volume 1 | Number 1 | Jan 2013 | Pages 1–100

Nanoscale

www.rsc.org/nanoscale

ROYAL SOCIETY OF CHEMISTRY

This is an *Accepted Manuscript*, which has been through the Royal Society of Chemistry peer review process and has been accepted for publication.

Accepted Manuscripts are published online shortly after acceptance, before technical editing, formatting and proof reading. Using this free service, authors can make their results available to the community, in citable form, before we publish the edited article. We will replace this *Accepted Manuscript* with the edited and formatted *Advance Article* as soon as it is available.

You can find more information about *Accepted Manuscripts* in the **Information for Authors**.

Please note that technical editing may introduce minor changes to the text and/or graphics, which may alter content. The journal's standard **Terms & Conditions** and the **Ethical guidelines** still apply. In no event shall the Royal Society of Chemistry be held responsible for any errors or omissions in this *Accepted Manuscript* or any consequences arising from the use of any information it contains.

www.rsc.org/nanoscale

Journal Name

ARTICLE

14.7% Efficient Mesoscopic Perovskite Solar Cells Using Single Walled Carbon Nanotubes/Carbon Composite Counter Electrode

Hao Li, Kun Cao, Jin Cui, Shuangshuang Liu, Xianfeng Qiao, Yan Shen, Mingkui Wang*

Single walled carbon nanotube (SWCNT) possesses excellent hole conductivity. This work communicates an investigation of perovskite solar cells using a mesoscopic TiO_2/Al_2O_3 structure as framework in combination with certain amount of SWCNT-doped graphite/carbon black counter electrode. The $CH_3NH_3PbI_3$-based device achieves a power conversion efficiency of 14.7% under AM 1.5G illumination. Detailed investigations show an increased charge collection in this device compared to that without SWCNT additive.

1. Introduction

Miyasaka et al. first demonstrated perovskite $CH_3NH_3PbX_3$ (X=Br, I) as an inorganic sensitizer in dye-sensitized solar cells in 2009.[1] Since organo-lead halide perovskite easily dissolves in polar solvents, it is not suitable for liquid electrolyte-based sensitized solar cells because of stability concerns. This instability problem can be solved by substituting a solid hole conductor for the liquid electrolyte.[2,3] Since then, organic-inorganic metal halide perovskite solar cells have received extensive attention due to their high power conversion efficiency (PCE) and low cost.[4] Most of efficient perovskite solar cell devices employ organic charge transfer materials, such as organic hole transport material (HTM) of 2,2',7,7'-tetrakis-(N,N-di-p-methoxy phenylamine)-9,9'-bifluorene (spiro-MeOTAD) [5] or electron transport material (ETM) of phenyl-C_{61}-butyric acid methyl ester (PCBM) [6] in combination with metal electrodes. The utilization of organic electronic components not only raises devices' cost but also affects their long-team stability. Thus, it is highly desirable to develop perovskite photovoltaics which are free of organic materials. Etgar et al first reported on a so-called HTM-free $TiO_2/CH_3NH_3PbI_3$ heterojunction solar cell showing a PCE of 8%.[7] In this device, the

Wuhan National Laboratory for Optoelectronics, Huazhong University of Science and Technology, Luoyu Road 1037, Wuhan 430074, P. R. China.
E-mail: mingkui.wang@mail.hust.edu.cn
Electronic Supplementary Information (ESI) See DOI: 10.1039/x0xx00000x

$CH_3NH_3PbI_3$ film on top of the mesoporous TiO_2 acts as light harvester as well as hole selective extraction layers at the same time. This type of perovskite solar cells photovoltaic performance depends on the depletion layer width at the $TiO_2/CH_3NH_3PbI_3$ junction.[8] A carbon counter electrode (CE) used for perovskite solar cell devices, collocated with a double layer of mesoporous TiO_2 and ZrO_2 as scaffold, has been exploited by Mei et al which achieves a PCE of 12.8%.[9] This work highlights a low cost, easy preparation and screen printable alternative electrode to replace noble metals electrodes.[10] $(5-AVA)_x(CH_3NH_3)_{1-x}PbI_3$ (5-AVA is 5-aminovaleric acid) acts as light harvester and hole conductor, which is penetrated into the 2 μm thick mesoporous TiO_2 and ZrO_2 layer. Such a thick absorber is superfluous if only for the purposes of light capture. The photo-generated holes have to travel over a relatively long pathway in such a structure before reaching the carbon CE. This leads to a misbalance between the effective light harvesting/charge transportation and effective isolation of the carbon conductive material from the TiO_2 electrode in perovskite solar cell devices using carbon CE.[8] An optimized thickness for a $CH_3NH_3PbI_3$-based perovskite solar cell is usually several hundred nanometers (~400 nm) thick due to its high light absorption ability (~10^5 mol cm^{-1}) and relatively long carrier diffusion length (~0.1-1 μm).[11,12] These important characteristics, which are related to $CH_3NH_3PbI_3$ preparation and device architecture, should be carefully utilized to optimize the device's PCE. Very recently, our group demonstrated ~15% efficient meso-structured perovskite solar cell based on inorganic scaffold, which employs a quadruple-layer architecture of mesoporous $TiO_2/Al_2O_3/NiO/C$.[13,14] This work emphasizes the importance of charge extraction in perovskite solar cell, thus improving devices' open-circuit voltage (V_{OC}) and output power ability.

Carbon nanotubes (both single-walled carbon nanotubes, SWCNTs, and multi-walled carbon nanotubes, MWCNTs) are excellent electronic transporting materials due to their exceptional charge transport feature as well as their chemical stability and

hydrophobicity. Carbon nanotubes have become one of promising components in perovskite solar cells. For example, Snaith *et al* demonstrated polymer-functionalized SWCNTs which can increase the thermal stability and the resistance of water for perovskite devices.[15] Mhaisalkar *et al* reported a perovskite solar cell fabricated with lamination of carbon nanotubes network film as hole collector, achieving a PCE of 6.87%.[16]

Here we show our findings on introduction of SWCNTs into carbon CE for mesoscopic structured perovskite solar cell devices. SWCNTs were selected for enhancing hole collection efficiency in this type of device due to its' 1D excellent conductor with highly hole mobility.[17] Most of SWCNTs have a diameter of 10-20 nm nanometer, with a tube length that can be many times longer. A PCE of 14.7% with an open-circuit voltage of 1.0 V has been achieved under standard testing condition for the mesoscopic structured perovskite devices using $CH_3NH_3PbI_3$ as light absorber in association with TiO_2/Al_2O_3/carbon as scaffold and SWCNTs/carbon composite as counter electrode. Compared to the pristine carbon CE, adding SWCNTs into carbon CE enhances charge separation and transport in $CH_3NH_3PbI_3$-based perovskite solar cell devices.

2. Experimental section

Material synthesis: CH_3NH_3I was prepared according to the literature process.[18] Briefly CH_3NH_3I was synthesized by adding 15 mL methylamine (40% in methanol, Aladdin) and 16.15 mL hydroiodic acid (57% in water, Aldrich) into a beaker at 0 °C with stirring for 2 hours. To precipitate CH_3NH_3I, the following step was used to remove solvents by rotary evaporation and the products were washed several times with diethyl ether. White crystals were obtained after drying in vacuum for 3 days.

SWCNTs were purchased from Shenzhen Nanotech Port Co. Ltd (NTP) with lengths less than 2 μm and an outer diameter distribution in 10-20 nm. The purity can reach 97 %. 1 g of SWCNTs was dispersed in 20 mL ethyl alcohol and sonicated in bath sonicator for 30 min, 0.588 g ZrO_2 (50 nm, Aladdin), 4 g graphite (8000 mesh) and 1 g carbon black (EC300) were added. This solution was treated with an ultrasonic probe for 5 min, then magnetic stirring 10 min, repeat these process three times. The mixture was subsequently centrifuged for 5 min at 4500 r/min to remove nonfunctionalized SWCNTs and other carbonaceous particles. The precipitate was recovered while the supernatant was discarded. The mixture was dispersed in ethyl alcohol, in which 17.6 mL terpilenol was added. The mixture was then treated by ultrasonic probe for 5 min, magnetic stirring 10 min, ball-milling 16 h. 2.94 g ethyecellulose was added in to the collection. In the last step, the ethyl alcohol was removed with rotary evaporation.

Device fabrication and characterization: Fluorine doped tin oxide (FTO) coated glass was etched with zinc power and 0.4 M hydrochloric acid. Then, the FTO glass was ultrasonically cleaned with detergent, water, deionized water and ethanol continuously. Subsequently, a 50 nm-thick compact TiO_2 layer was deposition onto the FTO substrate by spray pyrolysis deposition of titanium isopropoxide (trance metals basis, Aldrich) ethyl alcohol solution at 450 °C. After cooling to rooming temperature, a 400 nm-thick mesoporous TiO_2 nanocrystal film (30 nm-sized, Dyesol) was

deposited with screen printing, following with a 650 nm thick Al_2O_3 insulating layer (20 nm γ-Al_2O_3 nanoparticles, Aladdin). Then, an approximately 9~10 μm carbon paste (graphite/carbon black, 4:1, weight ratio) were subsequently printed on top of Al_2O_3 layer as counter electrode. The triple layer structure of (TiO_2/Al_2O_3/C) was sintered at 500 °C for 30 min. The deposition of $CH_3NH_3PbI_3$ into the TiO_2/Al_2O_3/C mesoscopic porous film was achieved by two-step sequential method [18-21] after the film cooling to room temperature. Firstly, 1.5 μL PbI_2 (500mg in 1 mL N,N-dimethylformamide (DMF)) was drop-coated onto the porous film and dried it at 70 °C. Then, the films were dipped into a solution of CH_3NH_3I dissolved in isopropanol (10 mg mL^{-1}) for 15 min. The film color changes from yellow to black, indicating the successful formation of $CH_3NH_3PbI_3$. For comparison purpose, a perovskite solar cell using spiro-OMeTAD as hole conductor and Au as counter electrode as fabrication according to previous report.[12]

The film thickness was measured with profile-meter (Veeco Dektak 150). The cross section of the sample was characterized with a field-emission scanning electron microscope (FE-SEM). The photocurrent-voltage (J-V) characteristics of the $CH_3NH_3PbI_3$-based solar cells were measured by recording the current through Keithley 2400 digital source meter. A xenon light source solar simulator (450W, Oriel, model 9119) with AM 1.5G filter (Oriel, model 91192) was used to give an irradiance of 100 mW cm^{-2} at the surface of the solar cells. The devices were tested using a metal mask with an area of 0.196 cm^{-2}. A similar data-acquisition system was used to control the incident photon conversion efficiency (IPCE) measurements. A white-light bias (10 % sunlight intensity) was applied onto the sample during the IPCE measurements with the alternating current (AC) model (10 Hz). The electronic impedance measurements (IS) were performed using the PGSTAT302N frequency analyzer from Autolab (The Netherlands) together with the Frequency Response Analyzer to give voltage modulation under the giving range of frequency. The Z-view software (v2.8b) was use to analyze the impedance data. The conductivity of the carbon counter electrode was determined with Van der Pauw four point probe measurements. The photovoltage/photocurrent transient decay (TPD) measurement was carried out to obtain the electron diffusion length (HuaMing, model 201501). A white light bias on the device sample was generated from an array of diodes. A ring of red light-emitting diode (LED) (Lumiled) was controlled by a fast solid-state switch. The pulse widths were 2 ms. Transients were measured at different white light intensities via tuning the voltage applied to the bias diodes. The voltage output was recorded on an oscilloscope directly connected with the cells.

3. Results and discussions

Figure 1a shows the schematic structure of a typical mesoscopic perovskite solar cell using TiO_2/Al_2O_3/C triple layer structure in association with $CH_3NH_3PbI_3$ light absorber. Herein, the TiO_2/Al_2O_3 mesoscopic film about 1 μm thick was covered by a ~10 μm mesoscopic carbon CE at the top of the device (Figure 1b). The $CH_3NH_3PbI_3$ was formed through drop-coating in combination with sequential deposition method. Since the mesoporous film is fully filled with $CH_3NH_3PbI_3$, it is difficult to identify the boundary between the TiO_2 and Al_2O_3 layers by SEM images.
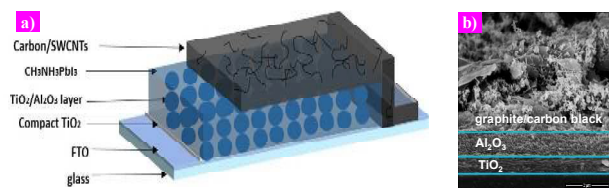
Fig. 1 (a) Schematic architecture of the investigated device consisting of FTO as a transparent substrate, a compact TiO_2 layer, a mesoporous TiO_2 layer, Al_2O_3 layer coated with SWCNTs added graphite/carbon black CE, (b) cross-section SEM image of mesoscopic perovskite solar cell.

Figure 2 shows optical images of contact-angle measurements with DMF on the carbon counter electrode before and after adding SWCNTs. Due to the strong hydrophobicity of SWCNTs, the acetylene blacks and graphite flakes composite film mixed by this additive (0.05%) exhibited a contact angle of 5° for DMF (Figure 2b), which is smaller than that of film without SWCNTs (being about 10 ^{o}). Consequently, a drop-dipping solution with DMF as solvent can easily spread and penetrate through the three-dimensional porous network, facilitating the pore-filling process. SWCNTs can be clearly observed between the small acetylene blacks and large graphite flakes (Figure S1). This connection may help to collect charges from $CH_3NH_3PbI_3$ to carbon. The porous carbon CE is beneficial for infiltration of PbI_2 and CH_3NH_3I to form $CH_3NH_3PbI_3$ (Figure S1b).
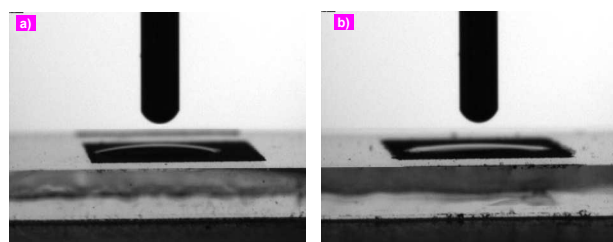
Fig. 2 Optical images of contact-angle measurements with N,N-dimethylformamide (DMF) on the carbon counter electrode with different content of SWCNTs (a) 0 % and (b) 0.05 %.

Some preliminary photovoltaic experiments were conducted to evaluate the performance of the new mesoscopic carbon counter electrodes devices containing SCWNTs with different concentrations. Figure S2 presents the J-V (reverse scan)and IPCE curves for devices A -D under standard AM 1.5G illumination at 100 mW cm^{-2}. Their photovoltaic parameters (V_{OC}, J_{SC} (short-circuit current), FF (fill factor), and PCE) are presented in Figure S3 by varying the SWCNTs content in CE. The devices with CEs containing 0, 0.02, 0.05, and 0.1% SWCNTs were labeled as A, B, C, and D, respectively. It was found that the V_{OC} and FF increased with SWCNTs, while the J_{SC} keeps almost constantly (Figure S3). The optimized device photovoltaic performance was observed at SWCNTs content of 0.05 % (device C). Figure 3a presents the J-V curves for devices A and C from different scan direction under standard AM 1.5G illumination at 100 mW cm^{-2}. A PCE up to 14.7% was achieved for device C with a V_{OC} of about 1 V, a J_{SC} of 21.26 mA cm^{-2}, and a FF of 0.69. Under the same condition, device A without SWCNTs in the CE exhibited a PCE of ~9.9% with a V_{OC} of 0.889 V, a J_{SC} of 20.26 mA cm^{-2}, and a FF of 0.55. For comparison purpose, a common perovkiste solar cell using spiro-OMeTAD as hole conductor and Au as counter electrode was measured and the photovoltaic parameters were presented in Figure 3 and Table 1. The device E with spiro-MeOTAD as the hole conducting layer shows a V_{OC} of 0.95 V, a FF of 0.67, and a J_{SC} of 20.83 mA cm^{-2} with a PCE of 13.3%. The device E performance with a standard spiro-MeOTAD/metal contact configuration can be further improved by optimization of film thickness and morphology. However, this is not the scope of this work. Table 1 also compares the photovoltaic parameters of these devices obtained from different scan direction under various temperatures. It is interesting that, comparing to devices using standard spiro-MeOTAD/metal contact CE, the main feature for perovskite solar cells using SWCNTs doped graphite/carbon black CE present much less photocurrent hysteresis effect. The photocurrent hysteresis was suggested to be caused by ion transport in $CH_3NH_3PbI_3$ under an external bias, rather than the ferroelectrics of $CH_3NH_3PbI_3$.[22,23] Figure 3b presents the correspond-ing IPCE curves of various devices. Devices A and C show a wide range photocurrent response with IPCE value over 60% from 350 nm to 750 nm and a maximum IPCE value approaching 80% from 500 nm to 650 nm. The IPCE value shown in the spectra is in good agreement with the J_{SC} as shown in Figure 3a. The increase of FF may be attributed to the increase of connection among the acetylene black and graphite flake as well as $CH_3NH_3PbI_3$ by the adding of SWCNTs. The average value of FF decreases distinctly when the content of SWCNTs increases up to 0.1 wt%. The fill factor was suggested to be correlated to the series resistance. However, it is interesting to note herein the composite counter electrodes with various SWCNTs content show similar values for square resistance (Table S1). Therefore, we argue that the increased FF in device C may not be caused by reducing sheet resistance. The addition of SWCNTs also helps the charge extraction as discussed below. Thus far, most of highly efficient perovskite solar cells (18-20%) are using organic electronic conductor and metal counter electrode as well additives, which are facing long term stability issue and moisture induced degradation. Even though perovskite solar cells using SWCNTs composite CEs in this study show less PCE (~14.7%), these devices shows highly promising in stability and low cost fabrication process.[24] This has been evidenced by other inorganic materials such as $CuSCN$[25], CuI[26], and NiO[27].
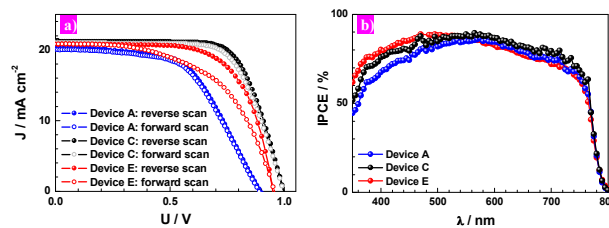
Fig. 3 (a) I-V curve of devices A, C and E with reverse scan (from V_{OC} to 0 V) and forward scan (from 0 V to V_{OC}) direction (scan rate 50 mV s^{-1}) under standard AM 1.5G illumination at 100 mW cm^{-2}. (b) The corresponding IPCE spectra of devices A, C, and E.

The work function of counter electrode plays critical role in hole extraction in this type of solar cell. Ultraviolet photoelectron spectroscopy (UPS) measurement was first performed for the characterization of work function of SWCNTs/carbon composite

counter electrodes. Figure 4a and Figure S4 present the UPS characterization results. The SWCNTs/carbon composite films A and C containing of 0% and 0.05% (weight ratio) exhibited a similar value for the onset energy ($E_i \sim 0.02$ eV). The cutoff energy ($E_{cut\text{-}off}$) can be evaluated to be 17.12 and 16.52 eV, respectively. Therefore, the corresponding work function (φ) was estimated to be 4.10 and 4.70 eV by using the equation of $\varphi = 21.21\text{-}(E_{cut\text{-}off}\text{-}E_i)$ for films A and C. This indicates a clear improvement of work function induced by addition of SWCNTs. Figure 4b shows an energy lever diagram for various components, allowing us to understand how the device works smoothly. The photo-induced electron transfers from $CH_3NH_3PbI_3$ (conduction band, CB, -3.8 eV) to the TiO_2 (CB, -3.9~-4.2 eV) while the hole transfers from $CH_3NH_3PbI_3$ (valence band, VB, -5.3 eV) to carbon.[21, 28-31]

Table 1 Summary of the photovoltaic parameters of the lead methyl-ammonium triiodide perovskite solar cells at room temperature.

a) Scan direction involving reverse scan (RS) and forward scan (FS).
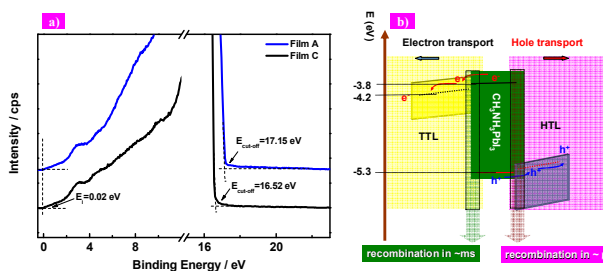
Fig. 4 a) The onset (E_i) and the cutoff ($E_{cut\text{-}off}$) energy regions of the surface measurement for the carbon CE with SWCNTs at 0 and 0.05% (wt%) (films A and C) from UPS characterization. b) The energy lever diagram of the investigated devices.

Figure 5 presents the relationship of V_{OC} as a function of logarithmic irradiation light intensity for devices A and C. The slope was evaluated to be 0.046 and 0.054/dec for devices A and C, respectively. In principle, the V_{OC} versus light intensity with a slope of $2kT/q$ (being 0.056/dec at room temperature) indicates bimolecular recombination in the interfacial charge transfer process.[21,32] A slope greater than $2kT/q$ means an additional interfacial trap-assisted Shockley-Read-Hall (SRH) recombination is involved. The bimolecular recombination refers to the recombination of free electrons and holes in the photoactive layer, while the monomolecular recombination refers to first-order process including the geminate recombination of a bound electron-hole pair before dissociation and the SRH recombination at the shallow traps created by defects and impurities in the interfacial layer. Therefore, we conclude that the free carrier recombination (bimolecular recombination) dominates the devices A and C. Figure S5 presents the J-V curve for device C under different light intensities. The device shows super linearity of efficiency with light density, reflecting that the charge collection of the devices is independent on light-intensity.

TPD measurements were further performed to examine the origin of the improved device characteristics, with which the charge-recombination lifetime and charge-extraction time can be obtained,

respectively. Figure 6a shows transient photocurrent decay for devices A and C serving as an example. The device C shows a faster carrier transport characteristic than that of device A. A fast charge transport ensures high charge collection, principally delivering higher output photocurrent. This can be caused by an improved connection among acetylene blacks, graphite flakes and $CH_3NH_3PbI_3$ when introduction of SWCNTs into carbon counter electrodes. The transient photocurrent decay curves can be fitted with a bi-exponential equation, indicating the presence of two distinguished population of generated carriers independently.[33,34] Thus, the electron and hole diffusion coefficients can be estimated to be 7.11×10^{-5} cm^2 s^{-1} and 7.36×10^{-5} cm^2 s^{-1} based on the transport lifetimes (τ_{t1} and τ_{t2} as shown in Figure 6b), respectively. This result is consistent with those obtained from photo-illumination spectroscopy measurements.[11,35] It is interesting to note that the hole diffusion coefficient is slightly increased to 7.85×10^{-5} cm^2 s^{-1} after

Device	Scan direction [a]	V_{oc} [V]	J_{sc} [mA cm^{-2}]	FF	PCE [%]
A	RS	0.889	20.26	0.55	9.9
A	FS	0.889	20.26	0.54	9.7
C	RS	1.01	21.26	0.69	14.7
C	FS	1.01	21.24	0.68	14.5
E	RS	0.947	20.83	0.67	13.27
E	FS	0.946	20.82	0.55	11.00

adding SWCNTs into the carbon counter electrode (filled symbols in Figure 6b). This can be attributed to the highly hole conducting property of SWCNTs.
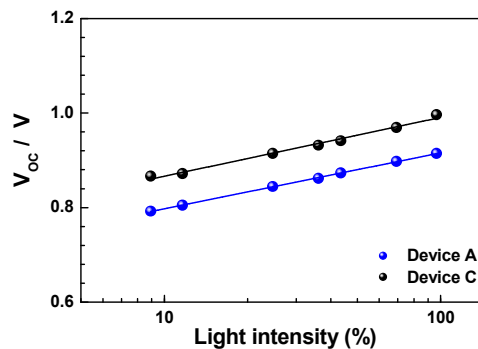
Fig. 5 Open-circuit voltage (V_{OC}) as a function of light-intensity for perovskite solar cells (devices A and C) with different concentration SWCNTs (0% and 0.05%) in carbon counter electrodes.

Likewise, the interfacial charge-recombination in the perovskite solar cells was further investigated with transient photovoltage decay measurement. Figure 6c presents the charge-recombination lifetime of devices A and C. The two recombination lifetime constants (τ_{r1} and τ_{r2}) are suggestive of the presence of two distinguished charge recombination kinetics (see Figure 4b).[36] A charge population bearing the short voltage decay component ($\tau_{r,2}$, filled, in the range of μs in Figure 6c) can be attributed to the electrons recombining with holes in SWCNTs near the $CH_3NH_3PbI_3$/carbon layer interface. And we associate the longer lifetime ($\tau_{r,1}$, empty, in the range of ms in Figure 6c) might be attributable to the charge confined within the

$CH_3NH_3PbI_3$ bulk layer recombining with defect traps or TiO_2.[12,13] The charge carrier transportation and recombination are schemed in Figure 4b. An increased lifetime $\tau_{r,2}$ was observed when SWCNTs were used. The lifetime $\tau_{r,2}$ for device C is about 2 times longer than that of device A. When considering the similar electron and hole diffusion coefficients as discussed above, a long charge lifetime guarantees effective charge collection efficiency, thus the device output photovoltage.[24] Indeed, about 80 mV enhancement in the V_{OC} was observed for device C compared with device A. Therefore, this result indicates that the augment in V_{OC} for device C could be contributed to the longer interfacial charge recombination lifetime at the $CE/CH_3NH_3PbI_3$ side.
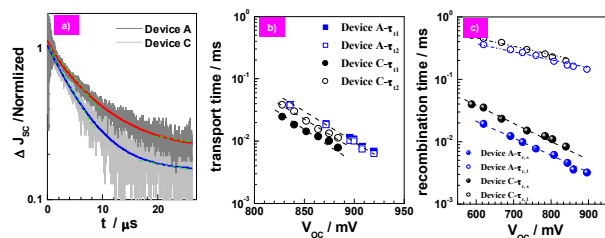
Fig. 6a (a) Transient photocurrent decay curves of devices A (dark gray) and device C (light gray) under short-circuit condition without white light bias. The solid lines are fitting curves with bi-exponential equation. (b) Transport time (τ_t), and (c) Recombination time (τ_r) date for devices A and C.

Electronic impedance spectroscopy (IS) characterization is a powerful tool to investigate the charge transport process and internal electrical properties in photovoltaic devices. Figure S6 shows the Nyquist plot of device A and C under illumination at a bias of -0.7 V in the frequency range of 4 MHz to 10 mHz. The frequency response shows three semicircles, representing three charge transfer processes. The semicircle in the high frequency regime corresponds to the electron transfer process between the TiO_2 and $CH_3NH_3PbI_3$ interface. The intermediate frequency semicircle represents the charge recombination process at the carbon $CE/CH_3NH_3PbI_3$ heterojunciton interface.[38] The semicircle in the low frequency is attributed to ionic motion in the $CH_3NH_3PbI_3$ layers.[25,33] We have fitted the IS data by a three series resistance capacitance (RC) circuits as showing in the inset of Figure S6.[22, 23, ,38-42] Thus, the interfacial recombination resistance (R_{CT}) and the charge exchange resistances (R_{CE}) can be obtained. As show in Figure 7a and b, device C shows relatively smaller charge transfer resistance (R_{CE}) and a shorter charge transfer lifetime. This result indicates better charge collection ability after the adding of SWCNTs. Figure 7c presents the interfacial recombination resistance (R_{CT}) as a function of bias for devices A and C. Fig. 7d shows the corresponding charge recombination lifetime $\tau_{r,l}$, which is determined from the recombination resistance (R_{CT}) and the geometrical capacitance (C) by $\tau_{r,l}=R_{CT} \cdot C$. The interfacial charge recombination rate (k) can be informed by the charge lifetime (τ_{r1}, $k \approx (\tau_{r1})^{-1}$), which is slightly inhibited when SWCNTs was added into carbon CE. This result agrees well with the transient photovoltage decay measurements (Figure 6c).
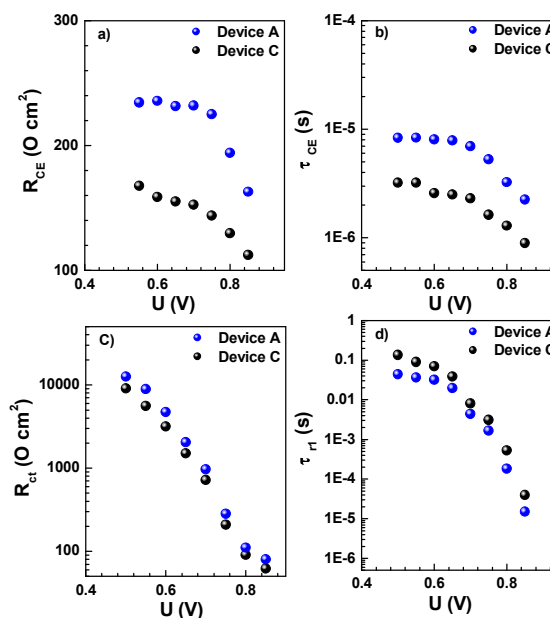
Fig. 7 Recombination, transport, and charge collection parameters as a function of voltage: (a) charge transfer resistance (R_{CE}); (b) charge transfer lifetime(τ_{CE}); (c) interfacial recombination resistance (R_{CT}) and (d) the corresponding charge recombination lifetime $\tau_{r,l}$ of Device A and C.

4. Conclusions

In summary, we have successfully fabricated the efficient mesoscopic perovskite solar cell using SWCNTs composite counter electrode. The optimized devices have achieved a power conversion efficiency of 14.7% with a V_{OC} up to 1 V. The incorporation of SWCNTs in carbon counter electrode modifies their working function and extends the charge recombination lifetime as well. Both are beneficial to the device photovoltaic performance, particularly the output photovoltage and fill factor.

Note and references

1. A. Kojima, K. Teshima, Y. Shirai, T. Miyasaka, *J. Am. Chem. Soc.* **2009**, *131*, 6050-6051.
2. J. Im, C. Lee, J. Lee, S. Park, N. Park, *Nanoscale*, **2011**. *3*, 4088-4093.
3. H. Kim, C. Lee, J. Im, K. Lee, T. Moehl, A. Marchioro, S. Moon, R. Humphry-Baker, J. Yum, J. Moser, M. Grätzel, N. Park, *Sci. Rep.,*. **2012**, *2*.
4. W. Yang, J. Noh, N. Jeon, Y. Kim, S. Ryu, J. Seo, S. Seok, *Science.* **2015**, *348*, 1234-1237.
5. P. Schulz, E. Edri, S. Kirmayer, G. Hodes, D. Cahen, A. Kahn, A. *Energy Environ. Sci.* **2014**, *7*, 1377-1381.

6. Q. Lin, A. Armin, R. Nagiri, P. Burn, P. Meredith, *Nat. Photon.* **2015**, *9*, 106-112.
7. W. Laban, L. Etgar, *Energy Environ. Sci.* **2013**, *6*, 3249-3253.
8. X. Xu, H. Zhang, K. Cao, J. Cui, J. Lu, X. Zeng, Y. Shen, M. Wang, *ChemSusChem.* **2014**, *7*, 3088-3094.
9. A. Mei, X. Li, L. Liu,Z. Ku, T. Liu, Y. Rong, M. Xu, M. Hu, J. Chen, Y. Yang, M. Grätzel, H. Han, *Science.* **2014**, *345*, 295-298.
10. A. Kay, M. Grätzel, *Solar Energy Mater. Solar Cells.* **1996**, *44*, 99-117.
11. S. Stranks, G. Eperon, G. Grancini, C. Menelaou, M. Alcocer, T. Leijtens, L. Herz, A. Petrozza, H. Snaith, *Science.* **2013**, *342*, 341-344.
12. S. Ma, H. Zhang, N. Zhao, Y. Cheng, M. Wang, Y. Shen, G. Tu, *J. Mater. Chem. A*, **2015**, *3*, 12139-12144.
13. X. Xu, Z. Liu, Z. Zuo, M. Zhang, Z. Zhao, Y. Shen, Z. Zhou, Q. Chen, Y. Yang, M. Wang, *Nano Lett.* **2015**, *15*, 2402-2408.
14. K. Cao, Z. Zuo, J. Cui, Y. Shen, T. Moehl, Z. Zakeeruddin, M. Graetzel, M. Wang, Nano Energy. **2015**, 17, 171-179.
15. S. Habisreutinger, T. Leijtens, G. Eperon, S. Stranks, R. Nicholas, H. Snaith, *Nano Lett.* **2014**, *14*, 5561-5568.
16. Z. Li, S. Kulkarni, P. Boix, E. Shi, A. Cao, K. Fu, S. Batabyal, J. Zhang, Q. Xiong, L. Wong, N. Mathews, S. Mhaisalkar, *ACS Nano* **2014**, *8*, 6797-6804.
17. M. Batmunkh, M. Biggs, J. Shapter, *Small.* **2015**, *11*, 2963-2989.
18. J. Burschka, N. Pellet, S. Moon, R. Humphry-Baker, P. Gao, M. Nazeeruddin, M. Grätzel, *Nature.* **2013**, *499*, 316-319.
19. N. Jeon, N. Noh, Y. Kim, W. Yang, S. Ryu, S. Seok, *Nat. Mater.* **2014**, *13*, 897-903.
20. Z. Liu, M. Zhang, X. Xu, F. Cai, H. Yuan, L. Bu, W. Li, A. Zhu, Z. Zhao, M. Wang, Y. Cheng, H. He, *J. Mater. Chem. A*, **2015**, *3*, 24121-24127.
21. K. Cao, J. Cui, H. Zhang, H. Li, J. Song, Y. Shen, Y. Cheng, M. Wang, *J. Mate. Chem. A.* **2015**, *3*, 9116-9122.
22. H. Zhang, X. Qiao, Y. Shen, T. Moehl, S. Zakeeruddin, M. Grätzel, M. Wang, J. Mater. Chem. A, 2015, 3, 11762-11767.
23. H. Zhang, X. Qiao, Y. Shen, M. Wang, J. *Energy Chem.* **2015**, doi:10.1016/j.jechem.2015.10.007.
24. J. Cui, H. Yuan, J. Li, X. Xu, Y. Shen, H. Lin, M.Wang, *Sci. Technol. Adv. Mater.*, **2015**, *15*, 036004.
25. S. Ye, W. Sun, Y. Li, W. Yan, H. Peng, Z. Bian, Z. Liu, C. Huang. *Nano Lett.*, **2015**, *15*, 3723-3728.
26. J. Christians, R. Fung, P. Kamat. *J. Am. Chem. Soc.,* **2014**, *136*, 758-764.
27. K. Wang, J. Jeng, P. Shen, Y. Chang, E. Diau, C. Tsai, T. Chao, H. Hsu, P. Lin, P. Chen, T. Guo, T. Wen. *Sci. Rep.*, **2014**, *4*, 4756.
28. Q. Wang, R. Wang, P. Shen, C. Li, Y. Li, L. Liu, S. Duhms, J. Tang, *Adv. Mater. Inter.* **2015**, *2*, 1400528.
29. J. Jeng, K. Chen, T. Chiang, P. Lin, T. Tsai, Y. Chang, T. Guo, P. Chen, T. Wen, Y. Hsu, *Adv. Mater.* **2014**, *26*, 4107-4113.
30. M. Lo, Z. Guan, T. Ng, C. Chan, C. Lee, *Adv. Funct. Mater.* **2015**, *25*, 1213-1218.
31. 24 V. Tung, J. Huang, J. Kim, A. Smith, C. Chu, J. Huang, *Energy Environ. Sci.* **2012**, *5*, 7810-7818.
32. Y. Yamada, T. Nakamura, M. Endo, A. Wakamiya, Y. Kanemitsu, *J. Am. Chem. Soc.* **2014**, *136*, 11610-11613.
33. V. Roiati, S. Colella, G. Lerario, L. De Marco, A. Rizzo, A. Listorti, G. Gigli, *Energy Environ. Sci.* **2014**, *7*, 1889-1894.
34. B. O'Regan, P. Barnes, X. Li, C. Law, E. Palomares, J. Marin-Beloqui, *J. Am. Chem. Soc.* **2015**, *137*, 5087-5099.
35. G. Xing, N. Mathews, S. Sun, S. Lim, Y. Lam, M. Grätzel, S. Mhaisalkar, T. Sum, *Science.* **2013**, *342*, 344-347.
36. J. Cui, C. Chen, J. Han, K. Cao, W. Zhang, Y. Shen, M. Wang, *Adv. Sci.,* **2015**, ADVS76.
37. J. Bisquert, L. Bertoluzzi, I. Mora-Sero, G. Garcia-Belmonte, *J. Phys. Chem. C.* **2014**, *118*, 18983-18991.
38. A. Dualeh, T. Moehl, N. Tetreault, J. Teuscher, P. Gao, M. Nazeeruddin, M. Grätzel, *ACS Nano.* **2013**, *8*, 362-373.
39. 35 E. Juarez-Perez, M. Wuβler, F. Fabregat-Santiago, K. Lakus-Wollny, E. Mankel, T. Mayer, W. Jaegermann, I. Mora-Sero, *J. Phys. Chem. Lett.* **2014**, *5*, 680-685.
40. V. Gonzalez-Pedro, E. Juarez-Perez, W. Arsyad, E. Barea, F. Fabregat-Santiago, I. Mora-Sero, J. Bisquert, *Nano. Lett.* **2014**, *14*, 888-893.
41. H. Kim, I. Mora-Sero, V. Gonzalez-Pedro, F. Fabregat-Santiago, E. Juarez-Perez, N. Park, J. Bisquert, *Nat. Commun.* **2013**, *4*, 2242.
42. Y. Zhao, A. Nardes, K. Zhu, *J. Phys. Chem. Lett.* **2014**, *5*, 490-494.

Nanoscale Accepted Manuscript